Ocean Dynamics (2016) 66:1429–1448
DOI 10.1007/s10236-016-0989-0

Turbulence-particle interactions under surface gravity waves

Mostafa Bakhoday Paskyabi[1]

Received: 13 May 2016 / Accepted: 29 August 2016 / Published online: 28 September 2016

Abstract The dispersion and transport of single inertial particles through an oscillatory turbulent aquatic environment are examined numerically by a Lagrangian particle tracking model using a series of idealised test cases. The turbulent mixing is incorporated into the Lagrangian model by the means of a stochastic scheme in which the inhomogeneous turbulent quantities are governed by a one-dimensional k-ε turbulence closure scheme. This vertical mixing model is further modified to include the effects of surface gravity waves including Coriolis-Stokes forcing, wave breaking, and Langmuir circulations. To simplify the complex interactions between the deterministic and the stochastic phases of flow, we assume a time-invariant turbulent flow field and exclude the hydrodynamic biases due to the effects of ambient mean current. The numerical results show that the inertial particles acquire perturbed oscillations traced out as time-varying sinking/rising orbits in the vicinity of the sea surface under linear and cnoidal waves and acquire a non-looping single arc superimposed with the high-frequency fluctuations beneath the nonlinear solitary waves. Furthermore, we briefly summarise some recipes through the course of this paper on the implementation of the stochastic particle tracking models to realistically describe the drift and suspension of inertial particles throughout the water column.

Responsible Editor: Bruno Castelle

✉ Mostafa Bakhoday Paskyabi
Mostafa.Bakhoday@uib.no

[1] Geophysical Institute, University of Bergen, and Bjerknes Center for Climate Research, Bergen, Norway

Keywords Stokes drift · Langmuir turbulence · Stochastic differential equation · Cnoidal waves · Solitary waves · Inertial particle

1 Introduction

The suspension and drift of buoyant particles, such as oil spills and biological matters, within an oscillatory turbulent fluid are frequently observed phenomena in a number of geophysical and offshore engineering applications (Murray 1970; Fowler and Knauer 1986; Wilson 2000; Ross 2010; Drivdal et al. 2014). While light particles, i.e., bubbles, exhibit strong tendency to trap in the high vorticity regions near the air-sea interface, heavy inertial particles (with diameter $>$ 200 μm) sink to the deep ocean due to their tendency to accumulate in the regions of high strain rate and low vorticity. They also have the ability to absorb and carry carbon into the water column (Noh et al. 2006; Fowler and Knauer 1986). Additionally, near the sea surface, the vertical dispersion and horizontal spreading of marine buoyant particles are substantially influenced by the wave-related processes such as the residual wave-induced flow (Stokes drift) which tilts the vertical vorticity toward the wave direction (Leibovich and Lumley 1999; Leibovich 1997). Therefore, the detailed knowledge of mechanisms controlling the transformation of water parcels subjected to wave and turbulent forces is essential to better understand the exchange physical, chemical, and biological processes (such as the global carbon cycle and pollutant distribution) across the air-sea boundary and throughout the water column.

Turbulence in the oceanic surface boundary layer, particularly in the regimes of breaking waves and coherent

large-scale Langmuir circulations, is one of the most important mechanisms which significantly controls the temporal and spatial distributions of tracers (Noh et al. 2006). The corresponding Lagrangian motions spread out across a wide range of scales from energy-containing (integral) scales on the order of mixed layer depth to the dissipative eddies of scales on the order of millimetres (Kolmogrov scale). Several local trapping (ejecting) events inside (from) these turbulent eddies occur for an inertial particle moving throughout the upper ocean mixed layer (Csandy 1963). Hence, the final state of the particle in such nonlinear system reveals a stochastic chaotic dynamics due to the inhomogeneities of the ambient flow. Such complexity of the underlying physics for the transportation of inertial particles in the disturbed turbulent flow can be captured theoretically through Langevin equations that relate the evolution of particle trajectories (velocities) to the stochastic forces acting on them. Wilson (2000) studied the dispersion of heavy particles in a turbulent flow using a simple Lagrangian Stochastic (LS) model. Noh et al. (2006) investigated the effects of turbulence on particle settling by analysing the motions of a large number of Lagrangian particles in the ocean mixed layer in the presence of Langmuir Circulations (LCs) (Craik and Leibovich 1976; McWilliams and Restrepo 1999). Jansons and Lythe (1998) studied analytically the stochastic effects on the Stokes drift of non-inertial particles when they are subjected to a Gaussian white noise. Jansons (2007) developed further the stochastic Stokes drift theory for inertial particles. Restrepo (2007) incorporated the effects of stochastic Lagrangian drift on the wave-driven circulation models by parameterizing the nonconservative wave breaking effects. Tang et al. (2010) calculated the stochastic Stokes drift for the monochromatic inertia-gravity waves and quantified the statistics of the various moments of the corresponding random process.

Several theoretical, numerical, and experimental studies have shown that the point particles underneath linear and nonlinear periodic waves experience non-closed orbits with horizontal drifts, and particles acquire a non-looping single arc during the passage of nonlinear solitary waves (Longuet-Higgins 1953; Bakhoday-Paskyabi 2015; Umeyama 2012). Nevertheless, the inertial particles extract momentum from the wave orbital motions near the air-sea interface and accelerate in the form of sinking/rising helix (Constantin 2006; Eames 2008; Santamaria et al. 2013). By moving from the sea surface towards the mid-water depth, other forces such as inertia and gravity start to deviate the particles from their trajectories induced by the dominant wave oscillatory motions. In most of the aforementioned studies, the main focus has been the extraction of inertial (point) particle motions within a non-turbulent flow in which the tracers follow the dynamics organised by the deterministic phase of fluid. In this study, the main objective is to investigate the dispersion of a single inertial particle beneath the irrotational linear, nonlinear, and solitary waves by accounting the intermittent and abrupt movements of particles perturbed by the turbulent diffusion processes. To prevent any difficulty raised for singling out the interactions between waves and inertial particles among other external active forces, we ignore the contributions from the mean current and implement the wave-component of instantaneous velocity field using the known analytical solutions of linear, nonlinear periodic, and solitary waves. Turbulent quantities in the water column are assumed either constant or determined from an Eulerian one-dimensional (1D) vertical ocean mixing model modified to include the wave effects (Bakhoday-Paskyabi et al. 2012; Bakhoday-Paskyabi and Fer 2014a).

The paper is structured as follows. In Section 2, we will give the background mathematical formulations associated to the surface wave field, fluid phase, and particle dispersal phase. A stochastic numerical solver is briefly explained in Section 3. We discuss numerical results in Section 4, and the final section includes some conclusions.

2 Mathematical formulations

2.1 Pure wave phase

2.1.1 Regular and irregular waves

Linear wave theory (i.e., small-amplitude wave theory) is the simplest possible water periodic wave theory for the surface gravity waves propagating over a constant depth D. By assuming no contributions from viscous and turbulent stresses (irrotational flow assumption), and too small wave steepness, $D/\lambda \ll 1$, where λ is the wavelength, the solution of linearized form of the two-dimensional Euler equations in the x-z plane results in the horizontal and vertical wave orbital velocities as

$$\tilde{u} = c\frac{\eta}{D}\cdot\frac{kD\cosh k(z+D)}{\sinh kD};\ \text{and}\ \tilde{w} = -c\eta_x\cdot\frac{\sinh k(z+D)}{\sinh kD}, \tag{1}$$

where $\eta = a\cos(\omega t - kx)$ is the surface elevation, a is the wave amplitude, ω denotes the angular frequency, k indicates the wavenumber, c is the phase speed, and η_x represents the surface slope (Svendsen 2006; Dean and Dalrymple 1992). An important advantage of linear theory (over nonlinear ones) is its potential to superimpose a finite

number of sinusoidal waves with different amplitude and random phase to simulate irregular sea surface. Thus, one can describe the water surface elevation as

$$\eta(x,t) = \sum_n \eta_n = \sum_n a_n \cos(\omega_n t - k_n x - \delta_n), \tag{2}$$

where δ_n is a random phase, and $a_n = \sqrt{2S_{\eta\eta}(f_n)\Delta f}$, in which $S_{\eta\eta}$ denotes the wave energy spectrum at frequency f_n. The wave energy spectrum may be obtained from either measurements or empirical relations, as well as numerically by solving the wave energy transport equation (Section 2.1.2). The wavenumber, k_n, and angular frequency ω_n at nth wave mode are related by the dispersion relation $\omega_n^2 = g k_n \tanh(k_n D)$, and the horizontal and vertical velocities of irregular waves are determined similar to Eqs. 1 and 2.

Due to inaccuracy of linear wave predictions in the presence of strong nonlinearity and large wave steepness, several nonlinear wave theories such as Stokes waves, small amplitude long waves, long waves from Boussinesq theory, and large amplitude long waves have been widely used to deal with the limitations of linear wave theory (Svendsen 2006). In this study, we use cnoidal waves which provide better estimations for wave propagation than the Stokes theory for the shallow water with moderate depth. The cnoidal waves are described by Jacobi's elliptic functions as the analytical solutions of Boussinesq equations (under some simplifications and approximations). The profile of surface elevation η in this theory is given by

$$\eta = \overbrace{\frac{h}{m}\left(1 - m - \frac{E(m)}{K(m)}\right)}^{\eta_2} + h\,\mathrm{cn}^2\left(2K\left[\frac{t}{T} - \frac{x}{\lambda}\right]|m\right), \tag{3}$$

where η_2 is the trough elevation, h is the cnoidal wave height, $K(m)$ and $E(m)$ are the complete elliptic integrals of the first and the second kind, m is the elliptic parameter, cn denotes the Jacobian elliptic function, and λ is the cnoidal wavelength. The horizontal and vertical cnoidal velocities are determined through:

$$\tilde{u} = \frac{1}{2}cD\left(\frac{1}{3} - \frac{(z+D)^2}{D^2}\right)\eta_{xx} + c\frac{\eta}{D} - c\left(\frac{\eta^2}{D^2} + \frac{\overline{\eta^2}}{D^2}\right), \tag{4}$$

$$\tilde{w} = -c(z+D)\left[\frac{\eta_x}{D}\left(1 - \frac{2\eta}{D}\right) + \frac{1}{6}D\left(1 - \frac{(z+D)^2}{D^2}\right)\eta_{xxx}\right], \tag{5}$$

where overbar denotes time-average over a wave cycle. In limiting case when $\lambda/D \to \infty$, the cnoidal solution approaches the solitary wave solution (Wiegel 1960; Whitham 1974; Svendsen 2006), see more details in Appendix A.

2.1.2 Wave-induced surface fluxes

The evolution of the surface directional energy spectrum can be obtained numerically, in the absence of the sea surface currents, by solving the wave energy transport equation:

$$\frac{\partial S_{\eta\eta}(f)}{\partial t} + \boldsymbol{c}_g \cdot \nabla S_{\eta\eta}(f) = S_{\mathrm{in}} + S_{\mathrm{ds}} + S_{\mathrm{nl}}, \tag{6}$$

where S_{in}, S_{ds}, and S_{nl} correspond to the wind input, dissipation, and nonlinear wave–wave interaction source terms, respectively, $\boldsymbol{c}_g$ is the group velocity, and ∇ is the two-dimensional horizontal gradient operator. The wave energy dissipated to the ocean, $\boldsymbol{\tau}_{wo}$, and the energy flux from the wind to the waves, $\boldsymbol{\tau}_{aw}$, are calculated from the following relations

$$\boldsymbol{\tau}_{aw} = \rho_w g \int_f S_{\mathrm{in}}(f)df; \quad \boldsymbol{\tau}_{wo} = \rho_w g \int_f S_{\mathrm{ds}}(f)df, \tag{7}$$

where ρ_w is the water density and S_{nl} integrates to zero across the whole frequency range.

2.2 Fluid phase

In this study, we only consider the contribution from the turbulence into the Lagrangian model by a diffusion term computed from a one-dimensional ocean mixing model as described in Bakhoday-Paskyabi and Fer (2014a). Components of temperature, salinity, and currents are computed on vertical sigma grids with refined resolution near the sea surface and bottom. Furthermore, the momentum equations are revised to include the wave effects by decomposing the instantaneous velocity vector, $\boldsymbol{u}$, into the mean, $\bar{\boldsymbol{u}}$, wave, and turbulence components, $\boldsymbol{u} = \bar{\boldsymbol{u}} + \boldsymbol{u}_s + \boldsymbol{u}'$ where $\boldsymbol{u}'$ represents the turbulent fluctuating velocity vector and $\boldsymbol{u}_s = (u_s, v_s, 0)$ is the Stokes drift vector given by

$$\boldsymbol{u}_s(z) = 2\int \omega k \hat{K} S_{\eta\eta}(f) \exp(-2k|z|)df, \tag{8}$$

where $\hat{K}$ denotes the wavenumber direction and k is the modulus of wavenumber. Here, the wave energy spectrum is calculated based on wave bulk information, H_s and T_p, from the empirical Joint North Sea Wave Project (JONSWAP) spectrum by assuming a fully developed sea.

2.2.1 General equations of motion

Using velocity decomposition for the incompressible turbulent flow, the equations of motion are obtained as

$$\frac{\partial \bar{u}}{\partial t} + \bar{u}\frac{\partial \bar{u}}{\partial z} + f_{\mathrm{Cor}}(\bar{v} + v_s) = -\frac{1}{\rho}\frac{\partial p}{\partial x} + F_{\mathrm{ds,x}} + \frac{\partial}{\partial z}(\overline{u'w'}), \quad (9)$$

$$\frac{\partial \bar{v}}{\partial t} + \bar{v}\frac{\partial \bar{v}}{\partial z} - f_{\mathrm{Cor}}(\bar{u} + u_s) = -\frac{1}{\rho}\frac{\partial p}{\partial y} + F_{\mathrm{ds,y}} + \frac{\partial}{\partial z}(\overline{v'w'}), \quad (10)$$

where p is the hydrostatic pressure, f_{Cor} is the Coriolis parameter, ρ is the mean density, and t denotes the time. $f_{\mathrm{Cor}}(u_s, v_s)$ is the Coriolis-Stokes force (CSF), and $\boldsymbol{F}_{ds} = (\boldsymbol{F}_{ds,x}, \boldsymbol{F}_{ds,y})$ are the dissipative forces induced by the wave breaking and wave-turbulence interaction (Bakhoday-Paskyabi et al. 2012). $\overline{u'w'}$ and $\overline{v'w'}$ are horizontal Reynolds stresses. Overbars denote time averaging.

The boundary condition at the sea surface due to the coupling between wind and wave forces is expressed by

$$\nu_t \frac{\partial \bar{\boldsymbol{u}}}{\partial z}|_{z=\eta} = \frac{1}{\rho_w}[\boldsymbol{\tau}_a - \boldsymbol{\tau}_{aw}], \quad (11)$$

where $\boldsymbol{\tau}_a$ is the total wind stress. A flux boundary condition is utilised at the bottom using the bottom stresses estimated from the log-law (Burchard et al. 1999).

2.2.2 Equations of TKE and its dissipation

The vertical mixing model in the presence of wave-turbulence interaction is computed using the following wave-modified k-ε scheme:

$$\frac{\partial E_k}{\partial t} = \frac{\partial}{\partial z}\left(\left(\nu + \frac{\nu_t}{\sigma_k}\right)\frac{\partial E_k}{\partial z}\right) + P_{\mathrm{shear}} + P_{\mathrm{Stokes}} + B - \varepsilon, \quad (12)$$

$$\frac{\partial \varepsilon}{\partial t} = \frac{\partial}{\partial z}\left(\left(\nu + \frac{\nu_t}{\sigma_\varepsilon}\right)\frac{\partial \varepsilon}{\partial z}\right) + \frac{\varepsilon}{E_k}(c_1 P_{\mathrm{shear}} + c_3 B + c_4 P_{\mathrm{Stokes}} - c_2\varepsilon), \quad (13)$$

where ν denotes the molecular diffusivity, $P_{\mathrm{shear}} = -(\overline{u'w'}\partial_z\bar{u} + \overline{v'w'}\partial_z\bar{v})$ and $B = -\nu_t'\partial b/\partial z$ are the shear production and buoyancy term, respectively, b represents the buoyancy vertical profile, and $P_{\mathrm{Stokes}} = -(\overline{u'w'}\partial_z u_s + \overline{v'w'}\partial_z v_s)$ indicates the Stokes production term.

The vertical diffusion of Turbulent Kinetic Energy (TKE), E_k, and its dissipation, ε, are denoted by the Schmidt numbers σ_k (here 1.3) and σ_ε (ranging from 0.8 to 1.11), respectively. $c_1 = 1.44$, $c_2 = 1.97$, $c_3 = 1$ if $B \geq 0$ and $c_3 = -0.52$ otherwise, and $c_4 = 1$ (Burchard 2002; Bakhoday-Paskyabi and Fer 2014a, b). Finally, the expressions for the eddy viscosity, ν_t, and diffusivity, ν_t', are given by $\nu_t = c_\mu E_k^2/\varepsilon$, and $\nu_t' = c_\mu' E_k^2/\varepsilon$, where c_μ and c_μ' are the so-called stability functions which depend on the shear, stratification, and turbulent time scale $\tau_t = E_k/\varepsilon$. We further use flux boundary condition for E_k at the sea surface as

$$\nu_t \frac{\partial E_k}{\partial z} = F_k, \quad (14)$$

where F_k prescribes the injection of turbulent flux from the wave field to the upper ocean (Bakhoday-Paskyabi and Fer 2014a, b). The flux boundary condition is used for ε at the first level below (above) the sea surface (bottom) using $\varepsilon = c_0^3 E_k^{3/2}/l$, where l is the turbulent length scale and $c_0 = 0.5544$ is an empirical constant. All wave-related modifications are implemented into the 1D General Ocean Turbulence Model (GOTM) (Burchard et al. 1999).

2.3 Particulate phase

The dispersed phase may be described by either an Eulerian or a Lagrangian approach. While in the Eulerian approach, a transport equation is governed for the continuum concentration field, the Lagrangian representation deals with a collection of transported particles as the dispersed phase of flow. The Lagrangian motion of a rigid spherical point-like particle at time t located at position $\boldsymbol{X}_p(t)$ with the total velocity of flow, $\boldsymbol{u}$, satisfies the equation:

$$\frac{d\boldsymbol{X}_p(t)}{dt} = \boldsymbol{u}(\boldsymbol{X}_p(t), t),$$

with the initial conditions $\boldsymbol{X}_p(0) = (x_p(0), y_p(0), z_p(0))$ at $t = 0$, and $\boldsymbol{u}$ is the superimposition of the background current and the wave-related motions, $\tilde{\boldsymbol{u}}$ in the absence of turbulence fluctuating motions. This equation holds only for passive tracers with a negligible size, $d_p \to 0$ where d_p is the particle diameter. These types of particles with the same density as the continuum phase are transported by the flow with no impact on the flow. However, the particles in several situations fail to follow the flow as a result of inertial effects. Point-like particles with a density smaller or larger than the surrounding fluid show completely different dynamics than passive tracers. While light particles ($\rho_p < \rho_f$) are accumulated in the regions of high vorticity, heavy particles exhibit tendency for tracing out from the vortex regions. To govern the translational motions of such inertial particles, Maxey and Riley (1983) developed a model for the motion of a small spherical rigid particle in an unsteady flow which in

the absence of Basset force, flow curvature, and lift induced by the velocity gradient can be expressed as

$$m_p \frac{d\boldsymbol{v}_p}{dt} = \overbrace{m_f \frac{D\boldsymbol{u}(\boldsymbol{X}_p(t),t)}{Dt}}^{1} + \overbrace{3\pi d_p \nu \rho_f [\boldsymbol{u}(\boldsymbol{X}_p(t),t) - \boldsymbol{v}_p]}^{2} + \overbrace{(m_p - m_f)g}^{3} + \frac{1}{2} m_f \left(\frac{D\boldsymbol{u}(\boldsymbol{X}_p(t),t)}{Dt} - \frac{d\boldsymbol{v}_p}{dt} \right), \quad (15)$$

where m_p and m_f are the masses of the particle and the displaced fluid, respectively, $\boldsymbol{v}_p(\boldsymbol{X}_p(t),t)$ denotes the particle velocity at position $\boldsymbol{X}_p$ and time t, ν is the kinematic viscosity of the fluid, and ρ_f and ρ_p are the fluid density and particle density, respectively. Term 1 is the acceleration of the fluid element at the position of the particle, term 2 is the so-called Stokes force acting on particles in a viscous flow. The third term represents the buoyancy force, and the last term is called the added-mass which accounts for the displacement of a certain amount of fluid when the particle moves relative to the fluid (i.e., the particle behaves as if it has an additional mass). This equation is valid for small particle Reynolds number, $Re_p = (d|v_p|)/\nu$. By accounting the terminal falling velocity, w_s, of the particle in the direction of gravity, Eq. 15 is then reduced to

$$\frac{d\boldsymbol{v}_p}{dt} = \beta_1 \frac{D\boldsymbol{u}}{Dt} + \frac{1}{\tau_p}(\boldsymbol{u} - \boldsymbol{v}_p - w_s \hat{\boldsymbol{z}}) + \beta_3 g, \quad (16)$$

where $\hat{\boldsymbol{z}}$ is the unit vector in the vertical direction, $\beta = \rho_p/\rho_f$, $\beta_1 = 3/(\beta+1)$, $\beta_3 = 2(\beta-1)/(2\beta+1)$, and $w_s = g(\beta-1)d_p^2/(18\nu)$. The response time of the inertial particle, τ_p, and the corresponding Stokes number, St, are given by

$$\tau_p = \beta_2 \frac{\beta d_p^2}{18\nu C_D} \quad \text{and} \quad St = \frac{\tau_p}{\tau_c}, \quad (17)$$

where $\beta_2 = (2\beta+1)/(2\beta)$, τ_c denotes a characteristic time scale of the fluid (i.e., the Kolmogrov time scale $\tau_c = \sqrt{\nu/\varepsilon}$ in a turbulent flow or gravity wave time scale for this study) and $C_D(Re_p)$ is a correction term for the non-Stoksian drag (here, we set $C_D = 1$ for the sake of simplicity). When $St \ll 1$, the particle is considered to be inertialess coupled to the continuous phase of flow. If $St \gg 1$, the particle can no longer adopt the dynamics of the flow and exhibits a different behaviour (Fowler and Knauer 1986).

2.3.1 Langevin model

So far, the trajectories of particles have been described by only the continuous phase of flow when there is no diffusivity or turbulence-induced perturbations along their trajectories. Under the influences of the vertical and horizontal turbulent dispersions, the buoyant particles are transported via random processes which are incorporated into the model by including an additive dispersal stochastic term. The two-dimensional motions of particles are then governed (in Itô form) through the Langevin equation (Kloeden and Platen 1999):

$$\frac{d\mathbf{X}_p(t)}{dt} = \boldsymbol{v}_p(\mathbf{X}_p(t)) + \nabla_* \mathcal{A} + \boldsymbol{\sigma}(\mathbf{X}_p(t),t)\frac{d\mathbf{W}_t}{dt}, \quad (18)$$

where the random process $\mathbf{X}_p(t) = (x_p(t), z_p(t))$ denotes the particle location, $\mathbf{W}_t$ is a vector of Wiener process at time t, i.e., the Wiener increments, $\mathbf{W}_{t+\Delta t} - \mathbf{W}_t$, are sampled as a normal distribution with mean 0 and variance Δt, and $\boldsymbol{\sigma} = \sqrt{2\mathcal{A}} = (\sqrt{2A_h}, \sqrt{2A_v})$ where $\mathcal{A} = 1/2\sigma \cdot \sigma^T$ is an indicator for the diffusion intensity and the diffusivity tensor, respectively. A_h and A_v are the horizontal and vertical turbulent mixing coefficients, respectively, (i.e., they are related to the turbulent eddy diffusivities and are different from the particle diffusivity). The first two terms on the right-hand side of Eq. 18 are called the drifts related to the kinetics of system, and the last term is called the diffusion describing the effect of stochastic noise. Itô interpretation, Eq. 18, is a diffusion process with transition conditional probability density, $P = P(s,x;t,z)$, satisfying the deterministic Fokker-Planck (FP) equation (or the backward Kolmogorov equation) which in the absence of the diffusivity gradient possesses the following form:

$$\frac{\partial P}{\partial t} + \boldsymbol{v}_p \nabla_* P = \frac{1}{2}\nabla_*^2(\boldsymbol{\sigma}^2 P), \quad (19)$$

where $\nabla_* = (\partial/\partial x, \partial/\partial z)$ denotes the spatial gradient differential operator with respect to x and z. Particle trajectory at each time t is determined by solving (19) together with proper spatial (Neumann) boundary conditions (Kloeden and Platen 1999). The most likely position of a particle at each time t is determined by minimising a likelihood function for evolution of particle position as a Markov process. In this study, instead of solving the deterministic equation (19), we numerically simulate (18) for time-step which is significantly smaller than the Lagrangian period, $\Delta t << T_L$. In the vicinity of areas where $T_L \to 0$, the numerical schemes for solving (18) require vanishingly small time steps. Therefore, we utilise small time steps for a Stochastic Range-Kutta (SRK) technique to relatively resolve this constraint for the known, continuous, and differentiable turbulent eddy diffusivity along the trajectories of particles.

3 Numerical methods

All Lagrangian trajectories in this study are calculated numerically using a four-stage Runge-Kutta method (RK), Appendix A. Therefore, we give a brief introduction on the general aspects of the numerical schemes for solving the Stochastic Differential Equations (SDEs).

The general form of solution for the d-dimensional SDE system in Itô representation (18) with a scalar Wiener process can be written using the following stochastic integral equation

$$\mathbf{X}_p(t) = \mathbf{X}_p(0) + \overbrace{\int_{t_0}^{t} \mathbf{f}(s, \mathbf{X}_p(s))ds}^{1} + \overbrace{\int_{t_0}^{t} \mathrm{g}(s, \mathbf{X}_p(s))d\mathbf{W}_s}^{2}. \tag{20}$$

with initial value $\mathbf{X}_p(t = 0) \in \mathcal{R}^d$ and $\mathbf{f}, \mathbf{g} : [0, t_N] \times \mathcal{R}^d \rightarrow \mathcal{R}^d$ are drift and diffusion functions, respectively, where $\mathcal{R}^d$ is the d-dimensional real number space. Term 1 is the conventional Reimann-Stelijes integral, and the second term is called Itô integral. Assuming a fixed time-step $\Delta t = (t_N - t_0)/N$, where $N > 0$ is a positive integer, and an equidistant partition of $[t_0, t_N]$ as $0 < t_1 < \cdots < t_N$, the discrete time approximation, $\mathbf{y}_t$, for the stochastic process $\mathbf{X}_p(t)$ at time t can be determined using the truncated Itô-Taylor series expansion:

$$\begin{aligned}\mathbf{y}_{t_{n+1}} &= y_{t_n} + \mathbf{f}(t_n, \mathbf{y}_{t_n})\mathbb{I}_{(0)} + \mathbf{g}(t_n, \mathbf{y}_{t_n})\mathbb{I}_{(1)} + \left[\mathbf{L}_g\mathbf{g}\right](t_n, \mathbf{y}_{t_n})\mathbb{I}_{(11)} \\ &\quad + \left[\mathbf{L}_g\mathbf{f}\right](t_n, \mathbf{y}_{t_n})\mathbb{I}_{(10)} + \left[\mathbf{L}_f\mathbf{g}\right](t_n, \mathbf{y}_{t_n})\mathbb{I}_{(01)} \\ &\quad + [\mathbf{L}_g^2\mathbf{g}](t_n, \mathbf{y}_{t_n})\mathbb{I}_{(111)} + \boldsymbol{\rho}(t_n, \mathbf{y}_{t_n}, \Delta t),\end{aligned} \tag{21}$$

where the residual term $\boldsymbol{\rho}$ satisfies $\mathbb{E}\{\boldsymbol{\rho}^2\} \approx \mathcal{O}((\Delta t)^4)$, $\mathbb{E}\{\cdot\}$ denotes the mean value of $\{\cdot\}$, and the differential operators, $\mathbf{L}_f$ and $\mathbf{L}_g$, are defined as follows:

$$\mathbf{L}_g = \sum_{i=1}^{d} g_i \frac{\partial}{\partial x_i}[\cdot],$$

$$\mathbf{L}_f = \sum_{i=1}^{d} f_i \frac{\partial}{\partial x_i}[\cdot] + \frac{1}{2}\sum_{i=1}^{d}\sum_{j=1}^{d} g_i g_j \frac{\partial^2}{\partial x_i \partial x_j}[\cdot].$$

The Itô stochastic integrals, $\mathbb{I}_{j_1 \cdots j_m}$, are expressed as

$$\mathbb{I}_{j_1 \cdots j_m} = \int_{t_0}^{t}\int_{t_0}^{\tau_m} \cdots \int_{t_0}^{\tau_2} \mathbf{y}(\tau_1) dW_{j_1}^{\tau_1} \cdots dW_{j_m}^{\tau_m},$$

where $dW_{j_i}^{\tau_i} = dW_{j_i}(\tau_i)$ for $i = 1 \ldots, m$, where m denotes the number of repeated integrals. As an example, some of the calculated Itô integrals are listed as follows

$$\begin{aligned}\mathbb{I}_{(0)} &= \Delta t, \mathbb{I}_{(1)} = \Delta W_n, \\ \mathbb{I}_{(01)} &= \Delta W_n \Delta t - \mathbb{I}_{(10)}, \\ \mathbb{I}_{(11)} &= \frac{1}{2}\left(\Delta W_n^2 - \Delta t\right),\end{aligned}$$

where ΔW_n indicates the 1D Wiener process increment. The numerical discrete approximation, Eq. 21, converges strongly to the exact solution $\mathbf{X}_p(t)$ at time t_N with constant order $p > 0$ if there exists a positive constant $C_p > 0$ such that

$$\mathbb{E}\{\|\mathbf{X}_p(t_N) - \mathbf{y}_{t_N}\|\} \leq C_p(\Delta t)^p, \tag{22}$$

where C_p is a coefficient independent of Δt. While by including further components of the Itô-Taylor expansion, higher order numerical schemes can be constructed, calculations of multiple stochastic integrals and their joint laws in the appeared higher order terms are very difficult and time-consuming. Therefore, a great deal of attention has been paid for developing derivative-free techniques such as SRKs due to their ease of programming, large stability regions, and flexible time-stepping strategy (Rößler 2010), see Appendix A.

4 Results

In this section, the sinking/swimming process of inertial particles is investigated in an oscillatory turbulent flow. The background mean current profile is neglected for all test cases due to our myopic focus on the interactions between waves and inertial particles. For simplicity, we assume that waves and wind field propagate in the same direction (i.e., in the x direction), and the Coriolis parameter is set for the latitude of 63°. The SDEs are implemented in Fortran codes by a non-adaptive SRK model performed on a MAC OS X 296 10.9.5 with Intel Core i7 3 GHz CPU, and 16 GB 1600 DDR3 RAM. The Mersenne Twister (MT) method is utilised to generate uniform pseudorandom numbers (Matsumoto and Nishimura 1998), and Box Muller transformation is used to transform the uniformly distributed random number sequences into the standard normal random values. We study the motions of inertial particles for homogeneous and non-homogeneous turbulent flows under various wind and wave forcing conditions. In the non-homogeneous case, the turbulent diffusion is determined from the numerical solutions of the wave-modified GOTM model along the trajectories of inertial particles using an interpolation technique. The stochastic-based displacements at each computational time, t, are determined by taking an ensemble average over a small number of realisations (i.e., 20 stochastic paths to speed up the computations). It is noted that for a small number of inertial particles (realisations), the stochastic models may not be able to properly capture the important features of underlying physics and their results would be directly dependent on the choice of random number generator, the selected value of SEED, and the value of time-step. The internal time-step for almost all simulation runs is set to $\Delta t = 0.005$ s (any change in the value of time-step will be reported wherever it is required). Meanwhile, the resuspenssion of particles near the surface boundary is governed using the reflecting boundary condition (see also Rose 2010). In order to investigate the inertial particles' responses to the turbulence-generated signals representative of both coastal and open ocean environments, we vary the strength of turbulence, identified here by the vertical eddy

diffusivity, A_z, from 0.05 (relatively weak) to 0.5 (strong) $m^2 s^{-1}$ for our idealised test cases. While near the air-sea interface and in the presence of buoyancy effect, the turbulence is statistically anisotropic, we simplify our analysis by assuming isotropic eddy diffusivity for the relatively small time scales (Batchelor 1970), i.e. $A_h = A_z$, in majority of test cases to highlight the role of vertical mixing in the dispersion of inertial particles, due to the fact that $A_z \ll A_h$.

It is worth to mention that for the non-homogeneous test cases, the effects of Stokes drift, under the mean sea level, in the horizontal/vertical excursion of inertial particles are (indirectly) accounted by the wave-modified fluid velocities as a result of including the effects of the CSF and the Stokes shear production in the momentum and energy equations. For more details about direct effects of Stokes drift on particles' motions, reader is referred to Bakhoday-Paskyabi (2015).

4.1 Lagrangian particles under homogeneous turbulence

In Fig. 1, three buoyant particles are launched at the same position at the sea surface, and expressions for the wave field are derived using the wind speed at 10 m height, U_{10}, from $H_s = 0.0248|U_{10}|^2$, $T_p = 0.729|U_{10}|$, and $a = H_s/2$ (Carter 1982). The trajectories are calculated by solving (16) and (18) for $St = 0.05$, $\beta = 1.05$, and different values of turbulent eddy diffusivities. Although in the deterministic case, the shapes of particles' trajectories are mainly governed by the initial conditions and parameter values (gray trajectories, see more details in Bakhoday-Paskyabi (2015)), the orbital looping-motions of inertial particles through the turbulent flow are significantly pronounced in the proximity of the air-sea interface. Particles exhibit a tendency towards a random state when they approach the deeper depths away from the surface as a function of wave conditions and the strength of turbulent mixing. Away from the surface, there are several local turning events where particles experience both trapping into the turbulent coherent structures and ejection from the turbulent eddies (Csandy 1963). Moreover, these crossing trajectory events may transport particles even opposed to the wave direction in a non-orbital paths because of the less required (Lagrangian) energy for the particles to move towards the negative direction. Additionally, we release two particles at 10 and 30 m below the sea surface in the presence of extreme level of turbulence intensity, i.e., $A_h = A_v = \mathcal{O}(10^{-2})$ (green line) and $A_h = A_v = \mathcal{O}(10^{-1})$ (brown line), respectively, in order to highlight the depth-dependency of particles' responses to the wave- and the turbulence-generated accelerations.

In Fig. 2, we present the influences of wave orbital motions on buoyant particles in a vertically homogeneous turbulent flow for three different values of $\beta = \rho_p/\rho_w$ and a fixed Stokes number, $St = 0.05$. Particles are released from the same locations at the surface with zero initial velocities for $A_v = A_h = 0.05$ m^2 s^{-1}. In the proximity of the surface boundary, particles acquire spiral motions whose frequency is equal to that of the wave's orbit. The strength of oscillatory modulations superimposed on the curling trajectory of particles are damped out as soon as particles approach deeper in the water column away from the wave's external forcing. The damping events, localized

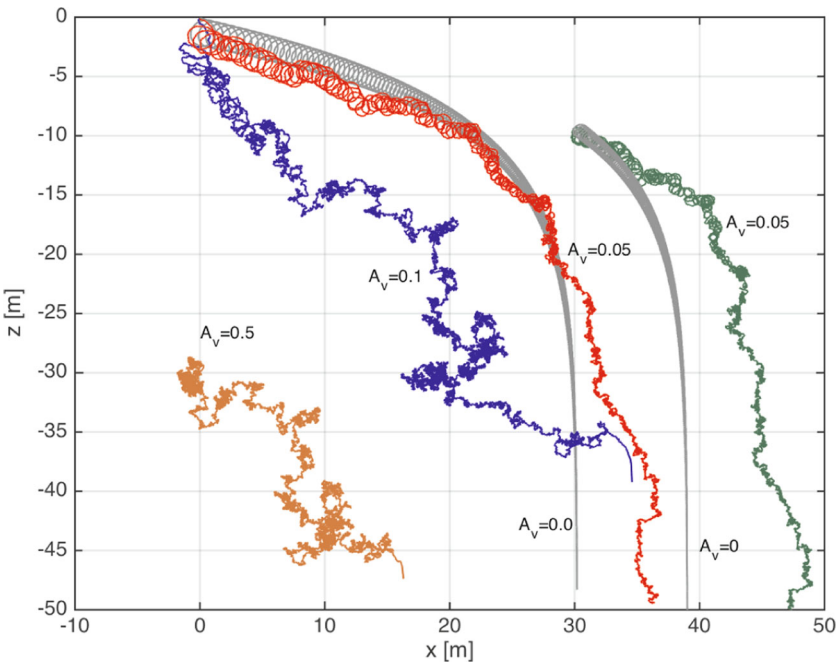

Fig. 1 The trajectories of inertial particles through turbulent flow under the influence of linear wave ($a = 1.25$ m, $T = 7.3$, and $D = 50$ m for $U_{10} = 10$ m s^{-1}). *Gray curves* show the deterministic simulation runs ($A_h = A_v = 0$ m^2 s^{-1}) for particles released at the sea surface and at 10 m below the surface. *Red* and *blue* trajectories indicate the mean trajectories of two heavy particles ($\beta = 1.05$ and $St = 0.05$) released at the sea surface with variances of 0.05 and 0.1 m^2 s^{-1}, respectively. *Green* and *brown curves* represent the mean trajectories of particles released at 10 and 30 m below the sea surface, respectively. The stochastic forces for these two particles have been set to 0.5 and 0.05 m^2 s^{-1}, respectively

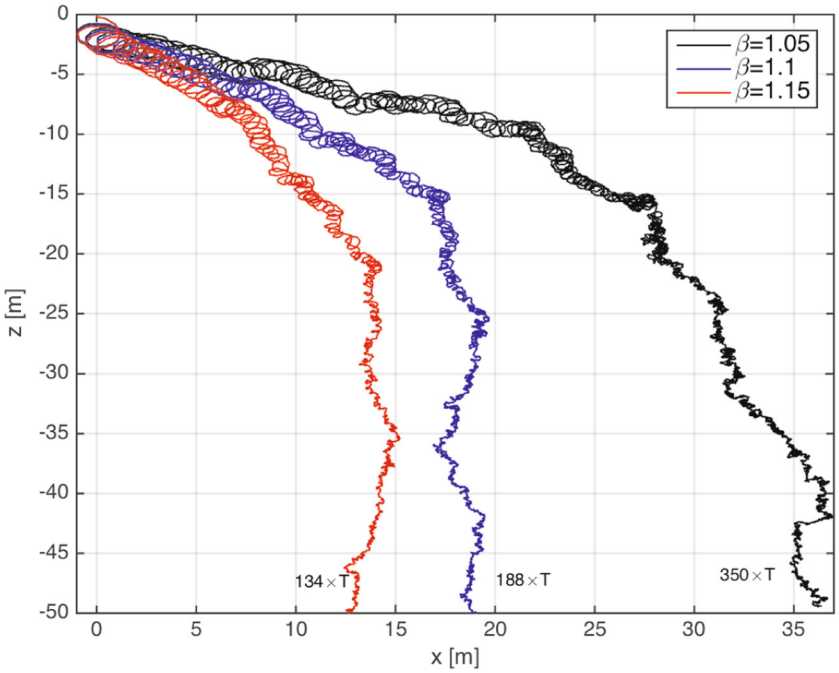

Fig. 2 Mean trajectories of three heavy particles with $St = 0.05$ and different values of $\beta = 1.05$ (*black*), 1.1 (*blue*), and $\beta = 1.15$ (*red*). Particles are released at the sea surface and are encountered with the uniform turbulence forcing, $A_h = A_v = 0.05\ \mathrm{m^2\ s^{-1}}$. Time-step and the total simulation time are $\Delta t = 0.005$ s and $350 \times T$ s, respectively. The linear wave period and amplitude are $T = 7.3$ s and $a = 1.25$ m, respectively. The water depth is set to $D = 50$ m

upwelling (particles' suspension), and downwelling (rapid sedimentation) become dominant mainly due to the emergence of other acting forces including inertia, added-mass, and buoyancy. As expected, the particle with $\beta = 1.05$ stays suspended for a longer time and travels longer horizontal distances than those with larger values of β.

Four light particles with different values of β and $St = 0.05$ released at the depth of 20 m disperse from their initial positions both diffusively and ballistically due to the linear wave oscillatory motions and background turbulent mixing (Fig. 3). Although particles are small enough to follow the instantaneous flow motions, they do not precisely mimic the wave oscillatory forcing. Because the coexistance of particle inertia and turbulent motions will result in a velocity nonequilibrium. The state of the velocity nonequibilirum enables particles to experience several trapping and ejecting events inside the turbulent eddies as a function of β and St due to the change of particles' residence time within

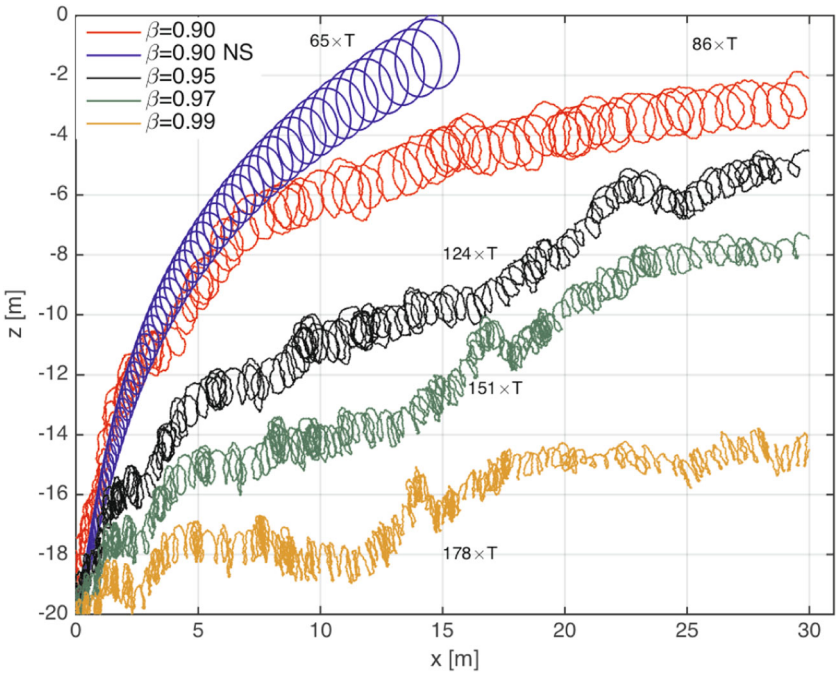

Fig. 3 Comparisons between mean trajectories of four light particles under the action of linear waves with $St = 0.05$ and different values of $\beta = 0.9$ (*blue* and *red*), 0.95 (*black*), 0.97 (*green*), and 0.99 (*brown*). Simulation runs are performed using $\Delta t = 0.005$ s for the total simulation time of $350 \times T$ s. Particle with $\beta = 0.9$ with No Stochastic (NS) forcing passes the free surface at times $65 \times T$ s. For the sake of better representation, we show and label the trajectories when particles travel the horizontal distance of 30 m. The water depth is $D = 20$ m and the wave parameters are the same as those used in the previous example

each turbulent eddies (so-called crossing trajectory effect, Csandy 1963). All light particles are dispersed in the direction of wave propagation and rise vertically through the turbulent flow. Furthermore, particles tend to remain suspended for a longer time with a specific distance from the sea surface than those with no stochastic variances (blue curve). This behavior is a result of applying the reflecting boundary condition at the sea surface.

In order to investigate how much the strength of stochastic forcing is able to influence the shape of the mean particles' trajectories under the influence of cnoidal waves, we vary the values of turbulent eddy diffusivity from zero variance ($A_h = A_v = 0$ m^2 s^{-1}) to $A_h = A_v = 1 \times 10^{-2}$ m^2 s^{-1}. Two particles with $\beta = 1.05$ and $St = 0.05$ are released at the sea surface (Fig. 4a). In zero stochastic dispersion case, particles acquire helical patterns near the wavy surface (black line) with a divergence from the trajectory imposed by the wave forcing as a function of depth. The effect of inhomogeneity, induced by the nonlinearity and stochasticity of the diffusion process, is reflected in the spatial distribution of particles and their relative excursion time compared with the deterministic pathway (Fig. 4a, red line). In Fig. 4b, we locate two light inertial particles at rest with $\beta = 0.95$ and $St = 0.05$ initially at the sea bed. As a response to the hydraulic forces (such as lift and drag depending on the particle's shape, size, and density) and wave oscillatory motions, they finally overcome the gravity and any other frictional forces by starting their horizontal and vertical excursions towards the sea surface. Through turbulent water which operates identically in all directions under the isotropy assumption, the inertial particle rises more slowly than it would through the non-turbulent water with an intermittency level dependent directly on the level of stochasticity and wave forcing (Fig. 4b, red line). Furthermore, due to using the reflecting boundary condition at the surface and the effects of nonlinearity, the light particle remains suspended in an almost certain distance from the surface for a long time.

Figure 5a illustrates the mean trajectories of two fluid particles (i.e., $\beta = 1$) being advected by a train of solitary waves for the various values of stochastic variances. For an identical (non-dimensional) horizontal and vertical diffusivities, the fluid particle experiences a random dispersion as a function of the (non-dimensional) wave amplitude, ζ, and the strength of the stochastic variance (blue and green lines). It is then suspended under the wave passage for a longer time (brown dashed line), and after passing one solitary wave cycle (black square markers) in a succession of separated solitary waves at the base of its non-looping orbit, particle governs a chaotic state of horizontal/vertical

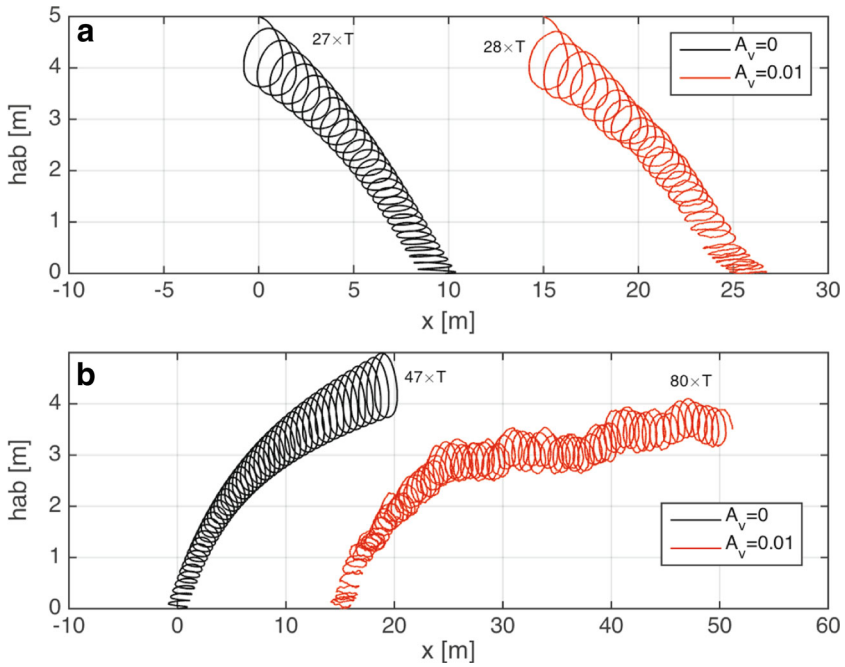

Fig. 4 **a** Mean trajectories of two inertial particles ($\beta = 1.05$ and $St = 0.05$) released at 5 m height above the bed (hab) under the influence of progressive cnoidal waves ($\mathcal{A} = 1.5$ m, $T = 7$ s and water depth of $D = 5$ m). The variances are set to $A_h = A_v = 0$ (*black curve*) for the deterministic case and $A_h = A_v = 1 \times 10^{-2}$ m^2 s^{-1} (*red curve*) for the stochastic case, respectively, and **b** mean trajectories of two light particles ($\beta = 0.95$ and $St = 0.05$) under cnoidal waves released at the flat bed. The *red curve* indicates the mean trajectory for the variance of 10^{-2} m^2 s^{-1} and the *black curve* represents the mean trajectory when the variance is set to zero. For the sake of clarity and reference, we plot the deterministic and stochastic trajectories 15 m horizontally away from each other. The time-step and the total simulation time are 10^{-2} and $100 \times T$ s, respectively. The number of realisations is set to 50 for these simulations

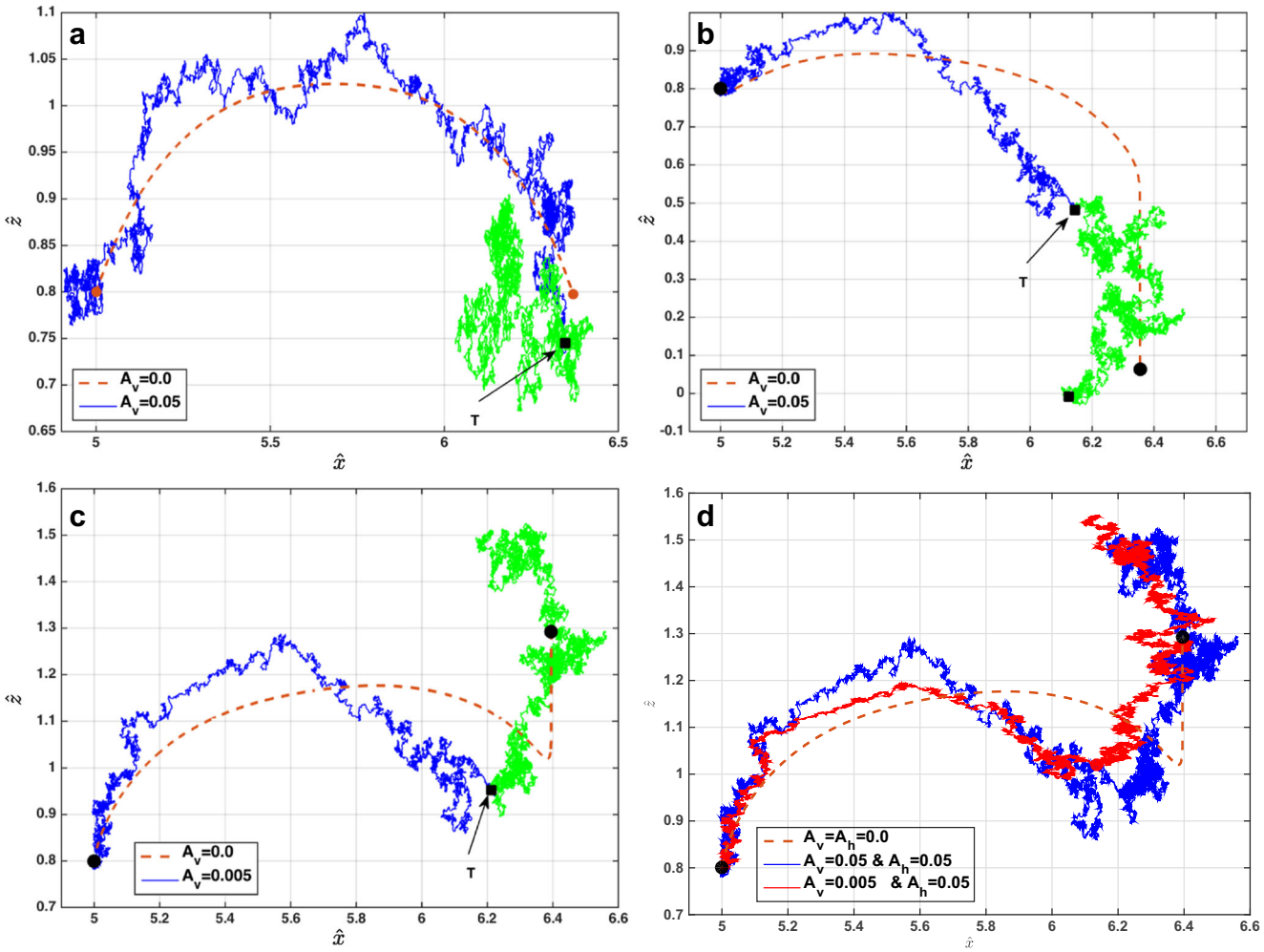

Fig. 5 The trajectories of particles under solitary waves for different stochastic forcing conditions. **a** Two point particles moving within the the homogeneous turbulent flow (i.e., $\hat{A}_v = \hat{A}_h = 0.05$) and within laminar flow; **b** dispersion of two heavy particles ($\beta = 1.05$ and $St = 0.05$) within the turbulent flow ($\hat{A}_v = \hat{A}_h = 0.05$) and within the non-turbulent flow; **c** two light particles ($\beta = 0.95$ and $St = 0.05$) moving through the turbulent flow ($\hat{A}_v = \hat{A}_h = 0.05$) and within the non-turbulent flow; and **d** three light particles dispersing within the laminar flow and turbulent flow with identical/non-identical horizontal and vertical eddy diffusivities. The water depth is 5 m for a solitary wave propagating with non-dimensional amplitude and reference simulation period of $\zeta = 0.35$ and $T = 10$, respectively. The reference simulation period is used for the full motion of the fluid particle on a single arc in the absence of stochastic forcing (*brown dashed curves*). We use 50 realisations for these simulations. The *arrows* show the locations of particles at one reference period T and *green curves* denote trajectories after one reference period. Furthermore, eddy diffusivities can be normalised using c_0 and D. See Appendix A for more details

displacements. In Fig. 5b, we investigate the effects of inertia on the mean trajectories of heavy particles ($\beta = 1.05$ and $St = 0.05$) under the action of different levels of stochasticity. Two similar inertial particles released at $\hat{z} = 0.8$, where $\hat{\cdot}$ denotes the non-dimentionalised depth, see Appendix A, advance horizontally-vertically after each period through a distance known as the drift or mass transport in the direction of wave propagation (Longuet-Higgins 1953; Bakhoday-Paskyabi 2015). As the variance of stochasticity increases, the mean trajectory deviates from the deterministic trajectory and the particle asymptotically approaches the end point of the deterministic pathway where it acquires long time traps due to the turbulent dispersal. Meanwhile, these heavy particles travel lower than they do for the fluid particles (i.e. Fig. 5a brown dashed line). Figure 5c shows that the non-looping motions of the light particles under the solitary waves are preserved for any level of stochasticity and particle inertia. We further study the effect of using non-identical horizontal and vertical diffusivities on the mean trajectories of light particles. Figure 5d shows the coupling between light particle's motions and the turbulence in which the extent of Brownian-like movements is directly linked to the strength of horizontal/vertical turbulent mixing. Although the generic behaviors for the movements

Table 1 Summary of experimental conditions ($T = T_p$ is the wave peak period)

EXP	U_{10} [m s^{-1}]	$u_s[ms^{-1}]$	$H_s[m]$	$T_p[s]$	$Q[Wm^{-2}]$	BC
1	15	0	0.0	0.0	0	NB
2	15	0.24	5.6	11.0	0	WB
3	15	0.24	5.6	11.0	+100	WB
4	15	0.24	5.6	11.0	−100	WB
5	10	0.0	0.0	0.0	0	NB
6	10	0.14	2.5	7.3	0	WB
7	10	0.14	2.5	7.3	100	WB
8	10	0.14	2.5	7.3	−100	WB

Here Q, NB, and WB stand for heat flux, with no wave breaking (NB) effect, and with wave breaking (WB) effect, respectively

of the point/buoyant particles have been analysed through conducting different numerical experiments, the trajectories may be polluted by the potential statistical outliers particularly when using too few realisations for calculating the ensemble-averaged pathway, and limitation of applying reflecting boundary condition at the surface.

4.2 Characteristics of the wave-induced vertical mixing

In order to investigate the impacts of Stokes drift and wave breaking on the vertical distribution of turbulent diffusion processes, we conduct eight numerical experiments as listed in Table 1. To extract the wave energy spectrum and Stokes drift profile (Fig. 6b) from the wind speed, we use the JONSWAP empirical spectrum in which the significant wave height and wave peak period are estimated from the empirical relationships suggested by Carter (1982). The model is set up for the water depth of 100 m with 80 m mixed layer depth separated from a homogeneous bottom layer by a thermocline thickness of 5 m and a temperature change of 5 °C (Fig. 6a). The temperature profile has a constant value of 20 °C above 80 m. In all simulation runs, the salinity is set constant, i.e., 35 ppt, and any density stratification is assumed due to the temperature gradients.

The effects of Stokes drift and surface heating/cooling in the structure of upper ocean mixing can be properly reflected in the vertical profile of turbulent eddy viscosity and diffusivity. Figure 7 illustrates different distribution of turbulent eddy viscosity for different experiments listed in Table 1. There exists a significant increase in the vertical profile of ν_t in depths ranged between 10 and 65 m when the synthetic impacts of Stokes drift and wave breaking are considered (Fig. 7b, black line) due to the wave-induced reduction in the amount of shear production

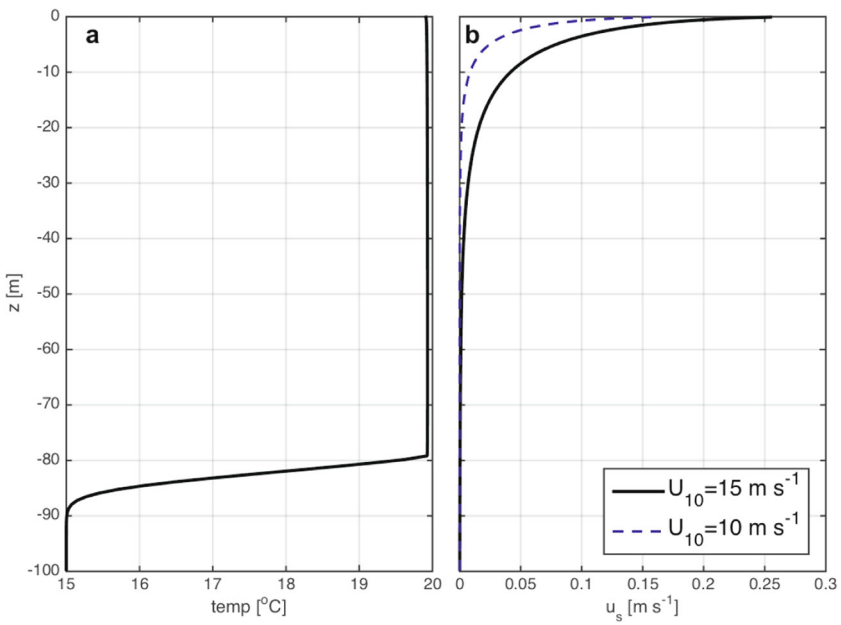

Fig. 6 Vertical profiles of **a** temperature and **b** Stokes drift computed from Eq. 8 using the wind speed and the JONSWAP empirical wave energy spectrum

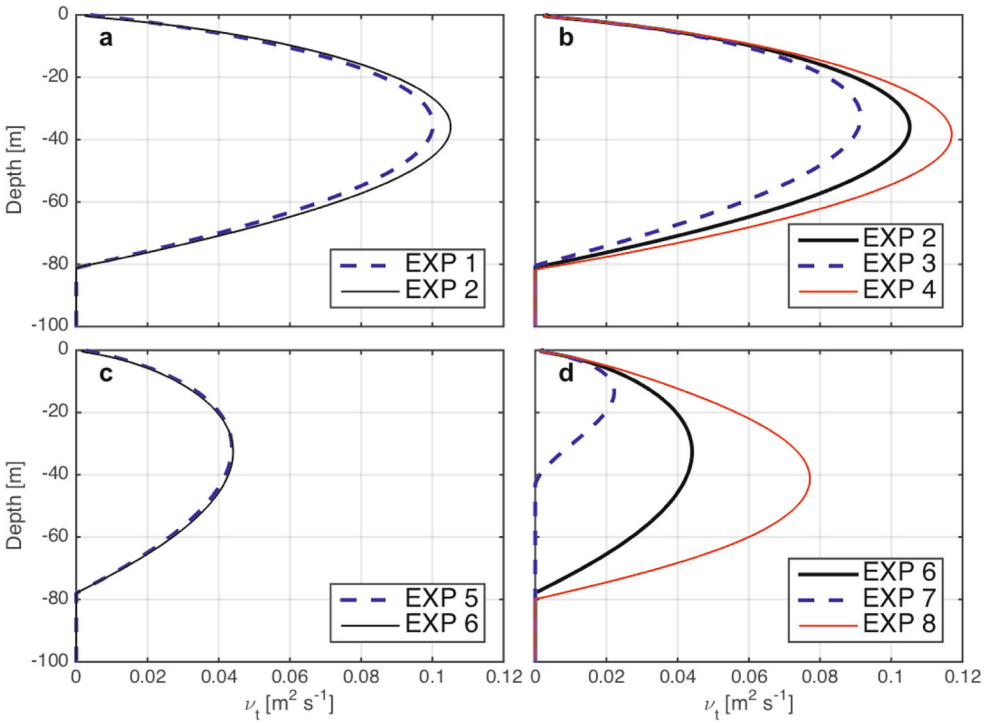

Fig. 7 The profiles of eddy viscosity from k-ε turbulence closure model for experiments listed in Table 1. Profiles of turbulent diffusivity for EXP4 and EXP6 will be shown in Figs. 8 and 9

near the sea surface. Furthermore, the contribution from the surface heating weakens the vertical mixing and strengthens the stratification by modulating the vertical distribution of turbulent eddy viscosity (dashed line). Alternatively, the combined effects of surface cooling, which destroys the stratification, and the wave effects will strengthen further the extent of mixing as shown in Fig. 7b, red line. Figure 7c and d similarly highlight the sensitivity of the vertical mixing to the surface forcing when wind speed drops from 15 to 10 m s^{-1}.

4.3 Langrangian particles in non-homogeneous turbulence

So far, the eddy diffusivity felt by inertial (or point) particles has been assumed constant for all test cases which may not be physically realistic in the presence of wind, wind-generated gravity waves, tides, and stratification. It is thus reasonable to consider vertically-varying eddy diffusivity to study how much the depth dependency of stochastic forcing is able to influence the shape of mean particles' trajectories. In the presence of particle inertia, the fluid fluctuating velocity may not necessarily be sensed by the fluid particles depending on the characteristics of dispersive phase such as the size, density, and geometry of particles. The discrepancy between the fluid turbulent diffusivity and the particle diffusivity or generally the decorrelation between continuous and dispersive phases results in significant changes in the geometry of heavy particles' paths, which will be briefly addressed in this section.

Vertical-horizontal distributions of particles from experiments 4 and 6 (Table 1) are shown in Fig. 8a and b for particles released at the sea surface under the action of linear waves. EXP4 and its corresponding turbulent diffusivity ($A_v = \nu_t'$, dashed brown line) can be regarded as a sum of wind- and wave-induced mechanical forcing, and thermal convective forcing caused by the buoyancy effect. The trajectories of three buoyant particles are shown for different values of β generated by the background oscillatory flow over the duration of $350\times T$ s, where T denotes the linear wave period. After being released at the sea surface, particles exhibit a typical tendency of greater horizontal excursions under the action of vertical diffusion profile and wave external forcing relative to the case of vertically uniform diffusivity (Fig. 2). The tendency for chaotic motions reaches its maximum value when vertical mixing is maximum at the depth of approximately 40 m. At the base of thermocline and very close to the sea surface and bottom where turbulent diffusion is negligible, particles acquire a complex geometry of localised upwelling and downwelling in response to all external forces particularly progressive wave orbital motions near the sea surface. Again, particles with smaller β stay suspended for a longer times and travel longer horizontal distances than those with larger β (Bakhoday-Paskyabi 2015). The vertical profile of eddy diffusivity in EXP6 shown in Fig. 8b corresponds to the only mechanical turbulence caused by the wind- and the wave-induced shear throughout the water column. In this experiment, wind speed drops from 15 to 10 m s^{-1}, and the fully developed wave field is generated correspondingly for

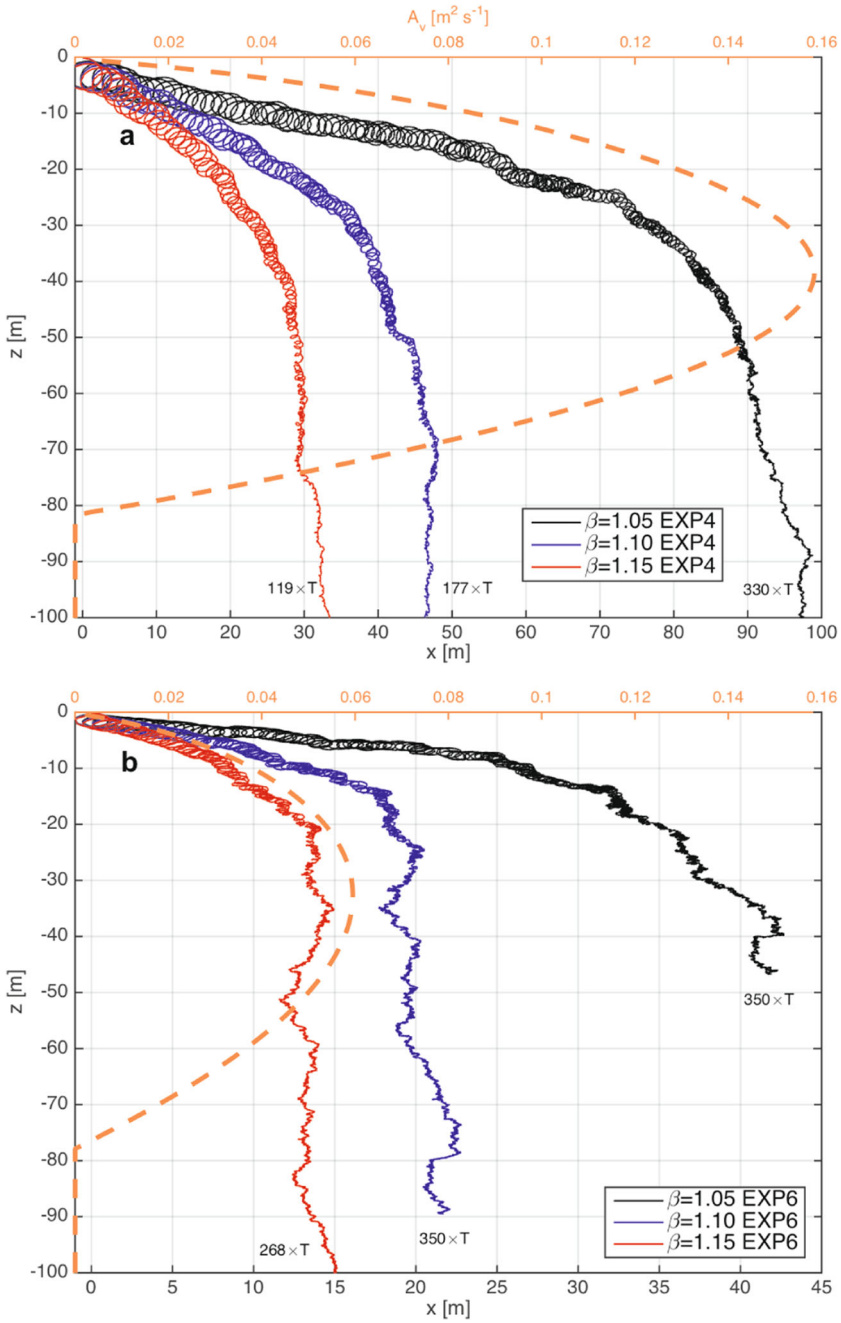

Fig. 8 Mean trajectories of three inertial particles with $St = 0.05$ and different values of β under the linear waves. The time-invariant and depth-dependent eddy diffusivities (*dashed brown lines*, labeled at top x-axis) are estimated for: **a** EXP4 and **b** EXP6 configurations. The total simulation time is $350 \times T$ and Δt is set to 0.005 s

U_{10} =10 m s^{-1} using JONSWAP spectrum. Three similar particles as shown in Fig. 8a are released in the proximity of the sea surface. While particles acquire the typical spiral motions, changes in the background oscillatory flow and in the vertical distribution of eddy diffusivity lead to particles experiencing rather slowly downward and forward displacements, as a result of staying inside the turbulent eddies over longer times (Fig. 8b).

The accurate description of stochastic forcing introduced by Eq. 18 depends also on the size of the time-step used in the discrete Wiener increments. Here, the ΔW_{t_n} is sampled from a Gaussian distribution $\mathcal{N}(0, 1)$ as $\Delta W_{t_n} = \sqrt{\Delta t}\mathcal{N}(0, 1)$. The pathwise information of the particle is then related to the choice of time-step size. Using strong convergence criteria in Eq. 22, it is clear that the estimated trajectory converges to the exact path as $\Delta t \to 0$. However, the effective choice of time-step can be achieved by accounting different processes, i.e., vertical and horizontal diffusivities, and other physical and biophysical processes. For example, in the presence of a stationary vertical diffusion process, the chosen time scale should be confined between the Lagrangian time scale of motions and $\partial_{zz}^{-1} A_v(z)$, where $A_v(z) = \nu_t'(z)$ denotes the vertical profile of 1D diffusivity. This parameter relates the accuracy of

Table 2 Summary of the CPU elapsed time for different values of β and Δt

β \ Δt [s]	10^{-4}	5×10^{-4}	10^{-3}	5×10^{-3}	10^{-2}
1.05	2984	604	304	63	30
1.15	2413	520	252	51	25

the Lagrangian tracking model to the GOTM vertical grid resolution, and the quality of the employed interpolation and smoothing schemes. Therefore, one should consider the sensitivity of the particle trajectory in the strong sense to the choice of time-step and the level of induced computational complexity. In Table 2, we demonstrate the CPU elapsed-time for different values of time-step and β. The elapsed-time climbs exponentially up when the step size decreases resulting in more efficient computational performance (in terms of computational demand) of the particle tracking method. It should be emphasised that any discontinuity in the turbulent diffusivity, in the presence of the diffusivity tensor effect (18), may constrain the model performance and accuracy, and increases significantly the computational cost of the stochastic scheme due to the need of the scheme to extremely small time-step size to preserve its convergency and stability. The elapsed-time analysis for the light particles are generally the same as that of obtained for $\beta > 1$ and is therefore excluded here for the sake of brevity.

The analysis of particle trajectories on the basis of linear and nonlinear regular waves ignores the influence of wave irregularity on the movements of particles. In Fig. 9, we assess the geometry of particles in an irregular oscillatory flow generated by the JONSWAP empirical spectrum and using Eq. 2. The effects of mean current and its superimposition with the wave field are also not taken into consideration. Figure 9 illustrates the trajectories of three particles with identical initial positions near the sea surface under the irregular waves. Underneath the irregular waves, particles experience the trapping and ejecting events with extended regions of stochastic excursions together with the less pronounced contributions from the wave-like motions compared with those under the regular waves in the proximity of the air-sea interface. This is because the turbulent vortex motions substantially interact with the wave field over a broad range of scales locally (inter-interactions between small scales) and non-locally (interactions between small and large scales). These interactions among different scales lead to very complicated patterns for the resonance and damping mechanisms acting on the coupled wave-turbulence-particle system with ability to change the degree of randomness and the variability of the small-scale processes within such a two-phase flow.

4.4 Lagrangian energy spectrum

The swimming/sinking trajectories of particles are closely related to the state of energy transfer in the turbulent flow under the local-isotropy assumption. These relationships are made through two broad classes of statistical diagnostics: those based on real space and those based on Fourier (wavenumber) space. The so-called structure functions (SFs) and correlation functions are two categories

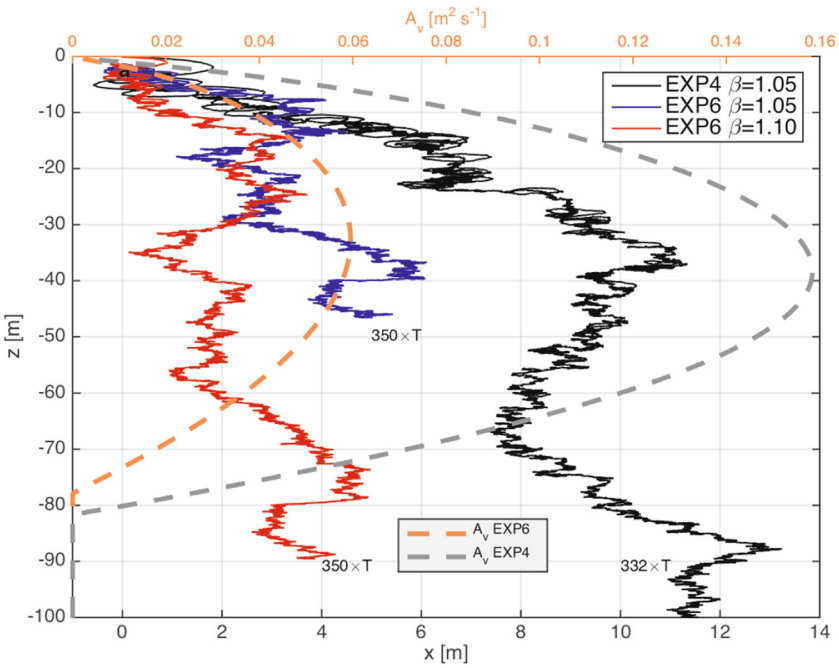

Fig. 9 The mean trajectories of three inertial particles for $St = 0.05$ and two values of β (i.e., 1.05 and 1.1) for EXP6 under the influence of the irregular (linear) waves. Here, $\Delta t = 0.005$ and the turbulent diffusivities are computed by the wave-modified GOTM model for EXP4 (only a single $\beta = 1.05$ for the sake of clarity) and EXP6 configurations

of real space statistical methods. Structure functions are determined from the time series of Lagrangian (here vertical) velocity along the trajectory of each (inertial) particle, $S_n^L(\tau) =< |w_p(t+\tau) - w_p(\tau)|^n >$, where the average is taken over time, τ is the time-lag, and n denotes the order of SF. Under the turbulence isotropy condition for valid ranges of frequencies, f, i.e., within the inertial subrange, the second-order SF (scaled by $\sim \tau$) corresponds to the f^{-2} power law and at frequencies beyond the inertial subrange, the spectrum falls in the dissipative subrange. Figure 10a shows the Lagrangian power spectra of vertical velocity from EXP4 and EXP6 calculated from Eq. 16. The effects of linear gravity waves in both cases are characterised by an energy elevation at the wave peak period (here, 11.0 s for EXP4 and 7.3 s for EXP6, respectively). Beyond this wave-affected frequency band, the Lagrangian velocity power spectrum is scaled as $\sim f^{-2}$. In the absence of turbulent mixing, the energy drops abruptly beyond the wave-affected subrange to the value of 10^{-9} with no pronounced inertial subrange (Fig. 10b, blue line). The discrepancies between the scaling exponent and the estimated Lagrangian energy spectrum may be interpreted as either the oversimplifications made for the calculations of Lagrangian trajectories, the quality of numerically generated stochastic processes, the inappropriate choice of time steps, or uncertainty in determining the wave-induced turbulent quantities.

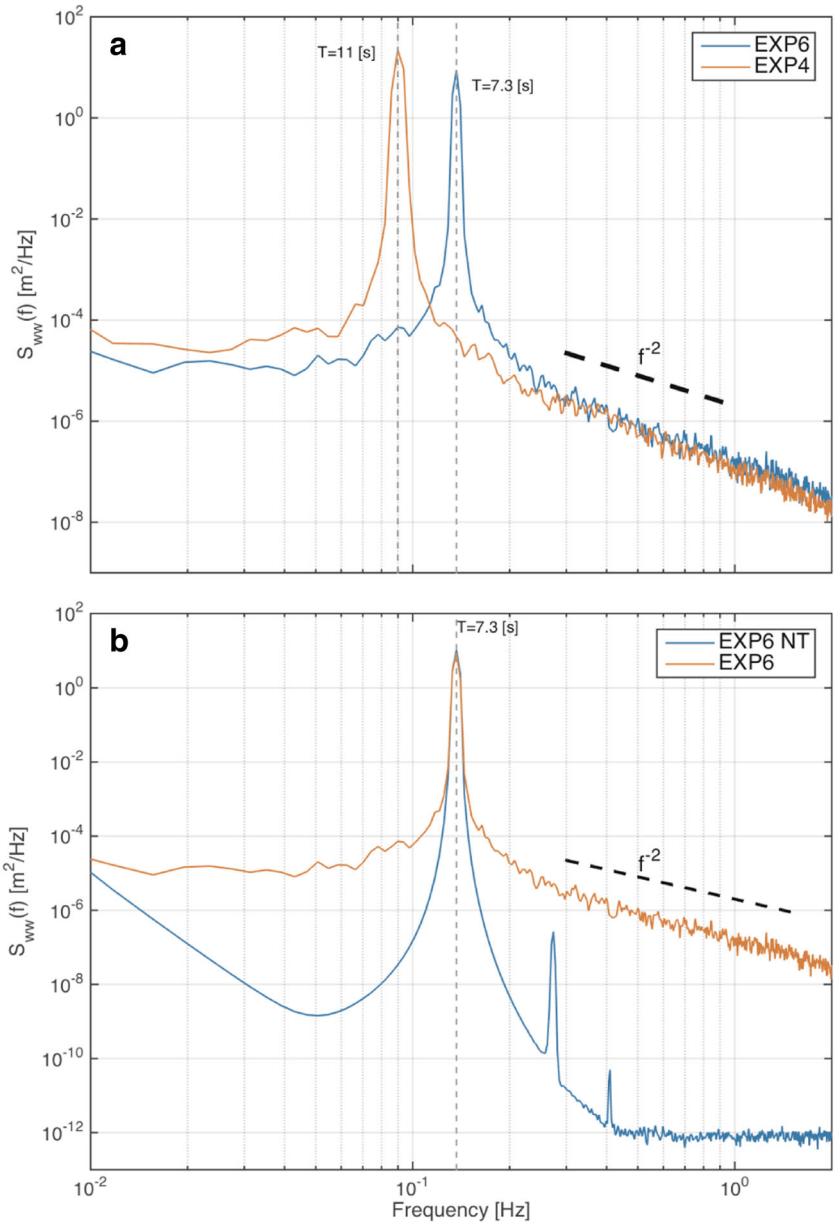

Fig. 10 Power spectra of the Lagrangian vertical velocities along the trajectories of the particles under the effect of progressive linear waves for: **a** eddy diffusivity estimated from EXP4 (*red*) and EXP6 (*blue*), respectively, and **b** eddy diffusivity from EXP6 (*red*), and simulation run with no-turbulence effect (NT, *blue*). Inertial subrange is characterised by the *dashed lines* with slop of −2. The time series of particle vertical velocity is extracted from Eq. 16

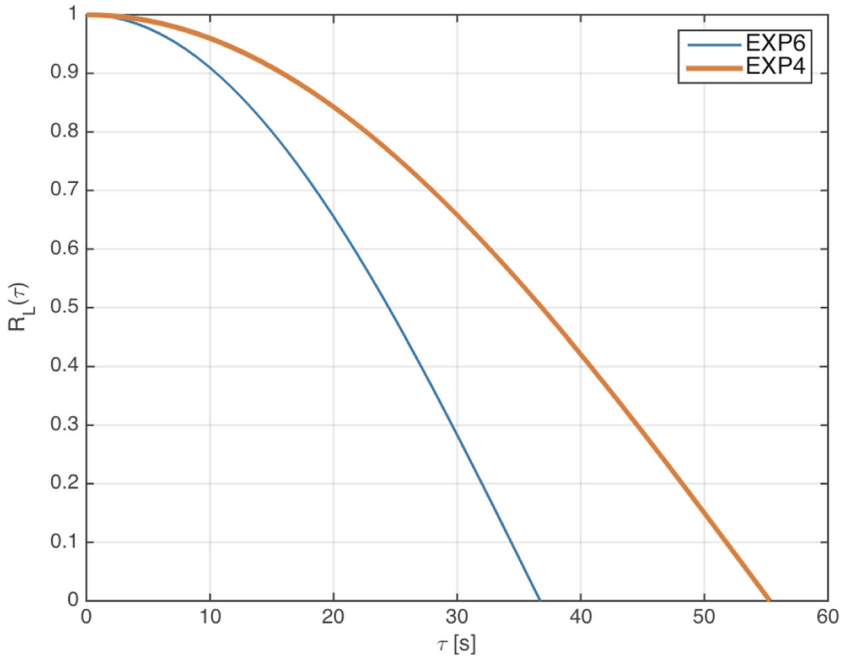

Fig. 11 Autocorrelations of the vertical velocity component (estimated from Eq. 16) for two heavy particles ($St = 0.05$ and $\beta = 1.05$) under the influence of linear waves. The turbulent diffusivities are computed by the wave-modified GOTM model for EXP4 and EXP6 configurations

Before closing this section, we present the Lagrangian auto-correlation (AC) function of the Lagrangian vertical velocity, $R_L(\tau)$, as

$$R_L(\tau) = \frac{\langle w_p(t) w_p(t+\tau) \rangle}{\langle w_p^2 \rangle},$$

with the time-lag of τ. The form of the AC function exhibits a general sharp drop to its first zero followed by damping oscillations due to the background wave oscillatory motions (not shown). We further find that the area under the graph of $R_L(\tau)$ before the first zero-crossing point is declined compared with the one in the pure isotropic turbulence in the absence of wave effects which influences the values of the Lagrangian integral time scale (Tennekes and Lumely 1972). Figure 11 shows the distinction of the Lagrangian integral time scales estimated from EXP4 and EXP6. As expected, the area under the graph of $R_L(\tau)$ before the first zero-crossing for EXP4 is larger than the one estimated from the EXP6 configuration.

5 Summary and conclusion

In this study, we investigated theoretically and numerically the motions of inertial particles in the ocean mixed layer by analysing the Lagrangian dynamics of a single inertial particle in a nontrivial turbulent flow field. The turbulence in a continuum-phase flow was predicted from a 1D hydrodynamic model modified to incorporate the effects of Coriolis-Stokes forcing, wave breaking, and Langmuir Circulation (LC). For the sake of simplicity, we neglected the effects of particles on the turbulent state of the carrier phase for all simulation runs. Our investigation was focused on determining the mean trajectory of inertial particles using a Lagrangian Stochastic (LS) model in the absence of the mean background current under the passage of linear (regular and irregular) and nonlinear (cnoidal and solitary) waves. By assuming the turbulence being isotropic at each point, the mean trajectories of inertial particles underneath all types of the aforementioned waves were examined by varying the relative strength of particles' heaviness, β, for a constant value of Stokes number, St. The results found are listed as follows:

1. Accurate choice of random number generator is the backbone of the LS models to substantially enhance the credibility of study by avoiding the injection of any incorrect dispersion into the solutions. In this study, we utilised the Mersenne Twister method to generate uniform random numbers and the Box-Muller transformation to produce the normal random numbers from the generated uniform random values.
2. Due to the turbulence-induced noise, the precision of higher-order Stochastic Differential Equation (SDE) solvers may be easily shaded so that the accuracy assessment between different discretization techniques is less practical.
3. This study considered only few trials of statistical trajectories in the ensemble-averaged pathway to focus in details on the interplay between waves, inertial particles and turbulence. For the realistic applications, the risk of statistical contaminations from using

too few inertial particles should be mitigated using sufficient number of particles.

4. The mean trajectories of inertial particles beneath progressive linear and nonlinear periodic waves exhibit strong oscillatory component, specifically close to the sea surface.
5. Under the solitary waves, the inertial particles preserve their non-looping motions when subjected to the chaotic turbulent coherence structures.
6. Including turbulent intensities results mostly in an increase in the residence time of inertial particles with respect to the quiescent conditions, at least for the conducted scenarios in this study.
7. Implementation of boundary conditions influences the trajectory of particles in the vicinity of surface and bottom boundaries (here we employed the reflecting boundary conditions). Therefore, the trajectories of particles will be modulated by modifying the boundary conditions.
8. The trajectories of inertial particles in the stratified turbulent flow differ from those in the isotropic turbulent flow because the trajectories of inertial particles reflect anisotropy of flow in their pathways.
9. The trajectories of inertial particles under irregular waves exhibit the extended regions of stochastic dispersions with less pronounced contributions from the orbital motions, particularly away from the air-sea interface.
10. The departure of Lagrangian power spectrum from the scaling exponent -2 at frequencies larger than the wave-affected frequency band may be explained by the intermittency and anisotropy of the oscillatory turbulent flow, and oversimplifications made in this study. Furthermore, the departure from the scaling exponent is substantially enhanced in our ideal simulations when the time series of particle vertical velocity are estimated from the finite differences of the particle vertical displacement. This necessitates further investigation which will be addressed in more details elsewhere.

The present work entailed a series of idealised test cases which cannot take into account various features of flow field, background turbulence, and particle dispersal motions. Therefore, the practical predictions of such complicated interactions need more sophisticated experiments by including different physical and biological processes in addition to the change of the strength of stochastic forcing or wave field characteristics. For more realistic problems, further investigations need to be conducted for the accurate choice of random number simulator, interpolation technique (interpolation of mean and turbulent quantities within the LS grid points), an appropriate degree of smoothing operator over the vertical (horizontal) diffusivity coefficients, the suitable number of particles, and the effective time-step size as a function of continuous phase characteristics and the properties of the dispersal phase.

Acknowledgment This work has been performed as part of the Norwegian Center for Offshore Wind Energy (NORCOWE) funded by the Research Council of Norway (RCN 1938211560) and by OBLO (Offshore Boundary Layer Observatory) project (RCN: 227777).

Appendix A: Particle trajectory for solitary waves

In this paper, the velocity fields for the solitary waves are associated to the exact solutions of the Korteweg-de Vries (KdV) equation. Let a be a typical wave amplitude, and L represents a typical horizontal length scale, the KdV equation is then approximated by the surface elevation for the wave motion predominantly in a single direction. By defining the following non-dimensional variables:

$$x \to Lx;\ z \to D(z-1);\ t \to L\frac{t}{c_0};\ \text{and}\ \eta \to \eta a,$$

where $c_0 = \sqrt{gD}$, the solitary solution for the non-dimensional KdV differential equation with the wave crest initially located at the origin is given by the following non-dimensional free surface equation:

$$\eta(x,t) = \zeta \operatorname{sech}^2\left[\sqrt{\frac{3\zeta}{4\xi}}\left(x - \left(1+\frac{\zeta}{2}\right)t\right)\right],$$

where $\zeta = a/D$ indicates the non-dimensional wave amplitude, $\xi = D^2/L^2$, and $0 \le z \le 1+\zeta\eta$. Using two different length scales, i.e., D and L, may result in difficulty for interpretation of the obtained results. Therefore, we introduce a new set of non-dimensional coordinates as

$$\hat{x} = \frac{x}{\sqrt{\xi}};\ \hat{z} = z;\ \text{and}\ \hat{t} = \frac{t}{\sqrt{\xi}}.$$

The horizontal and vertical velocity components are hence approximated in new coordinates using change of variable as follows

$$\hat{u}(\hat{x},\hat{t}) = \zeta\left[\psi(x,t) - \frac{z^2}{2}\xi\psi_{xx}(x,t) + \mathcal{O}(\xi^2)\right],$$

$$\hat{w}(\hat{x},\hat{t}) = \frac{\zeta}{\sqrt{\xi}}[-\xi z\psi_x(x,t) + \mathcal{O}(\xi^2)].$$

Following Whitham (1974), ψ can be estimated as a function of η:

$$\psi(x,t) \sim \eta - \frac{1}{4}\zeta\eta^2 + \frac{1}{3}\xi\eta_{xx}.$$

The resulting (non-dimensional) horizontal and vertical velocity components at an arbitrary point $(\hat{x},\hat{z})$ at a certain time $\hat{t}$ can be then estimated in terms of horizontal velocity at a fixed level θ from the even bottom using Taylor expansion of ψ about θ, i.e.:

$$\begin{aligned}\hat{u}(\hat{x},\hat{z},\hat{t}) &= \frac{\zeta}{4}\mathrm{sech}^2(\Theta)\left\{4+\zeta[4-7\mathrm{sech}^2(\Theta)]\right.\\ &\quad -3\zeta\hat{z}^2[2-3\mathrm{sech}^2(\Theta)]\\ &\quad +\frac{3}{2}\zeta^2(\theta^2-\hat{z}^2)[35\mathrm{sech}^4(\Theta)-34\mathrm{sech}^2(\Theta)+4\\ &\quad \left.-3\theta^2(15\mathrm{sech}^4(\Theta)-15\mathrm{sech}^2(\Theta)+2)]\right\},\\ \hat{w}(\hat{x},\hat{z},\hat{t}) &= \sqrt{3}\zeta^{3/2}\hat{z}\mathrm{sech}^2(\Theta)\tanh(\Theta)\\ &\quad \times\left\{1-\frac{1}{2}\zeta\mathrm{sech}^2(\Theta)-3\zeta\left(\frac{1}{3}-\frac{\theta^2}{2}\right)\right.\\ &\quad \left.\times(3\mathrm{sech}^2(\Theta)-1)\right\},\end{aligned}$$

where $\Theta=\sqrt{3\zeta/4}(\hat{x}-c\hat{t})$ where $c=1+\zeta/2$, and the solutions of $d\hat{x}/d\hat{t}=\hat{u}$ and $d\hat{z}/d\hat{t}=\hat{w}$ lead to an estimation for the non-dimensional trajectory of a particle passing through a laminar flow (Bakhoday-Paskyabi 2015). It is worth to mention that the velocity field for the two-parameter KdV equation depends only on a single parameter, i.e., ζ, for solitons.

Appendix B: Stochastic Runge-Kutta scheme

A s-stage stochastic Runge-Kutta scheme for the numerical solution of the Itô SDE (20) is written as follows (Rößler 2010):

$$\begin{aligned}\mathbf{y}_{t_{n+1}} &= \mathbf{y}_{t_n}+\Delta t\sum_{j=1}^{s}\alpha_j\mathbf{f}(t_n+\mu_j^{(0)}\Delta t,Y_j^{(0)})\\ &\quad +\sum_{j=1}^{s}\gamma_j\mathbf{g}(t_n+\mu_j^{(1)}\Delta t,Y_j^{(1)}),\end{aligned}\tag{23}$$

for $n=1,\ldots,N$ with the following stages

$$\begin{cases}Y_i^{(0)}=\mathbf{y}_{t_n}+\Delta t\sum_{j=1}^{s}a_{ij}^{(0)}\mathbf{f}(t_n+\mu_j^{(0)}\Delta t,Y_j^{(0)})+\sum_{j=1}^{s}b_{ij}^{(0)}\mathbf{g}(t_n+\mu_j^{(1)}\Delta t,Y_j^{(1)})\frac{\mathbb{I}_{(10)}}{\Delta t},\\ Y_i^{(1)}=\mathbf{y}_{t_n}+\Delta t\sum_{j=1}^{s}a_{ij}^{(1)}\mathbf{f}(t_n+\mu_j^{(0)}\Delta t,Y_j^{(0)})+\sum_{j=1}^{s}b_{ij}^{(1)}\mathbf{g}(t_n+\mu_j^{(1)}\Delta t,Y_j^{(1)})\sqrt{\Delta t},\end{cases}\tag{24}$$

where $i=1,\ldots,s$, $B^{(0)}=[b_{ij}^{(0)}]_{s\times s}$ and $B^{(1)}=[b_{ij}^{(1)}]_{s\times s}$ are random matrices, and

$$\gamma^T=\left[\gamma^{(1)}\mathbb{I}_{(1)}+\gamma^{(2)}\frac{\mathbb{I}_{(11)}}{\sqrt{\Delta t}}+\gamma^{(3)}\frac{\mathbb{I}_{(10)}}{\Delta t}+\gamma^{(4)}\frac{\mathbb{I}_{(111)}}{\Delta t}\right]_{1\times s},$$

is a random vector including four diffusion coefficients $\gamma^{(1)}$, $\gamma^{(2)}$, $\gamma^{(3)}$, and $\gamma^{(4)}$. $A^{(0)}=[a_{ij}^{(0)}]_{s\times s}$, $A^{(1)}=[a_{ij}^{(1)}]_{s\times s}$, and $\alpha^T=[\alpha_i]_{1\times s}$ are matrices and drift vector associated with the deterministic components, respectively. While such strong approximations have been mainly constructed for Strotonovich representation of SDEs (Burrage and Burrage 1996), Rößler (2010) recently introduced a derivative-free SRK for path-wise approximation (strong order of 1.5) with the corresponding Butcher tableau for $s=4$ shown as follows (SDRK4). This class of strong order 1.5 for the stochastic elements results in a strong order of 2 for the drift term. One of important advantages of this strong approximation with respect to those introduced by Kloeden and Platen (1999) is their substantial reduction of computational complexity for achieving the higher order of convergence.

(SRK4)

$\mu^{(0)}$	$A^{(0)}$	$B^{(0)}$	
$\mu^{(1)}$	$A^{(1)}$	$B^{(1)}$	
	α^T	$\gamma^{(1)^T}$	$\gamma^{(2)^T}$
		$\gamma^{(3)^T}$	$\gamma^{(4)^T}$

$=$

0				
$\frac{3}{4}$	$\frac{3}{4}$			
0	0	0		
0	0	0	0	
0				
$\frac{1}{4}$	$\frac{1}{4}$			
1	1	0		
$\frac{1}{4}$	0	0	$\frac{1}{4}$	
	$\frac{1}{3}$	$\frac{2}{3}$	0	0

$\frac{3}{2}$			
0	0		
0	0	0	
$\frac{1}{2}$			
-1	0		
-5	3	$\frac{1}{2}$	
-1	$\frac{4}{3}$	$\frac{2}{3}$	0
2	$-\frac{4}{3}$	$-\frac{2}{3}$	0

-1	$\frac{4}{3}$	$-\frac{1}{3}$	0
-2	$\frac{5}{3}$	$-\frac{2}{3}$	1

When the diffusion term approaches to zero, $\mathbf{g} \rightarrow 0$, soluion of Eq. 20 is reduced to the deterministic RK method (DRK). In this study for the deterministic ODEs, we use standard 4-stage DRK (DRK4) with the following Butcher tableau:

$$
\text{(DRK4)}\quad
\begin{array}{c|c|c}
\mu^{(0)} & A^{(0)} & B^{(0)} \\
\hline
 & \alpha^T & \gamma^{(0)^T}
\end{array}
=
\begin{array}{c|cccc|cccc}
0 & 0 & 0 & 0 & 0 & 0 & 0 & 0 & 0 \\
\frac{1}{2} & \frac{1}{6} & 0 & 0 & 0 & 0 & 0 & 0 & 0 \\
\frac{1}{2} & 0 & \frac{1}{2} & 0 & 0 & 0 & 0 & 0 & 0 \\
1 & 0 & 0 & \frac{1}{2} & 0 & 0 & 0 & 0 & 0 \\
\hline
 & \frac{1}{6} & \frac{1}{3} & \frac{1}{3} & \frac{1}{6} & 0 & 0 & 0 & 0
\end{array}
$$

References

Batchelor GK (1970) The theory of homogeneous turbulence. Cambridge University Press

Bakhoday-Paskyabi M (2015) Particle motions beneath irrotational water waves. Ocean Dyn 65:1063–1078

Bakhoday-Paskyabi M, Fer I (2014a) Turbulence structure in the upper ocean: a comparative study of observations and modelling. Ocean Dynamic, doi:10.1007/s10236-014-0697-6

Bakhoday-Paskyabi M, Fer I (2014b) The influence of surface gravity waves on the injection of turbulence in the upper ocean. Nonlin Proc Geophys 21:713–733

Bakhoday-Paskyabi M, Fer I, Jenkins AD (2012) Surface gravity wave effects on the upper ocean boundary layer: modification of a one–dimensional vertical mixing model. Cont Shelf Res 38:63–78

Burchard H (2002) Applied turbulence modelling in marine water. Springer, p 100

Burchard H, Bolding K, Villarreal MR (1999) GOTM, a general ocean turbulence model: theory, implementation and test cases. Space Applications Institute

Burrage K, Burrage PM (1996) High strong order explicit Runge-Kutta methods for stochastic ordinary differential equations. Appl Numer Math 22:81–101

Carter DJT (1982) Prediction of wave height and period for a constant wind velocity using the JONSWAP results. Ocean Eng 9:17–33

Constantin A (2006) The trajectories of particles in Stokes waves. Invent Math 166:523–535

Craik ADD, Leibovich S (1976) A rational model for Langmuir circulations. J Fluid Mech 73:401–426

Csandy GT (1963) Turbulent diffusion of heavy particles in the atmosphere. J Atmos Sci 20:201–208

Dean RG, Dalrymple RA (1992) Water wave mechanics for engineers and scientists. Prentice-Hall Inc, Englewood Cliffs

Drivdal M, Broström G., Christensen KH (2014) Wave-induced mixing and transport of buoyant particles: application to the Statfjord oil spill. Ocean Sci 10:977–991. doi:10.5194/os-10-977-2014

Eames I (2008) Settling of particles beneath water waves. J Phys Oceanogr 38(12):2846–2853

Fowler JD, Knauer GA (1986) Role of large particles in the transport of elements and organic compounds through the oceanic water column. Prog Oceanogr 16:147–194. doi:10.1016/0079-6611(86)90032-7

Jansons KM (2007) Stochastic Stokes' drift with inertia. Proc R Soc. doi:10.1098/rspa.2006.1778

Jansons KM, Lythe GD (1998) Stochastic Stokes' drift. Phys Rev Lett 81:3136–3139

Kloeden PE, Platen E (1999) Numerical solution of stochastic differential equations. Springer, Berlin

Leibovich S, Lumley JL (1999) A theoretical appraisal of the joint effects of turbulence and of Langmuir circulations on the dispersion of oil spilled in the sea. US Coast Guard Office of Research and Development Report CG-D-26-82, Washington, DC, p 119

Leibovich S (1997) Surface and near-surface motion of oil in the sea. Report to US Minerals Management Service, Contract 14-35-0001-30612

Longuet-Higgins M (1953) Mass transport in water waves. Philos Trans Roy Soc London 245:535–581

Maxey MR, Riley JJ (1983) Equation of motion for a small rigid sphere in a nonuniform flow. Phys Fluids 26.4:883–889

Matsumoto M, Nishimura T (1998) Mersenne twister: A 623-dimensionally equidistributed uniform pseudorandom number generator. ACM Trans Model Comput Simul 8(1):3–30. http://www.math.sci.hiroshima-u.ac.jp/m-mat/MT/emt.html

McWilliams JC, Restrepo JM (1999) The wave driven ocean circulation. J Phys Oceanogr 29:2523–2540

Murray SP (1970) Settling velocities and vertical diffusion of particles in turbulent water. J Geophys Res 75:1647–1970

Noh Y, Kang IS, Herold M, Raasch S (2006) Large eddy simulation of particle settling in the ocean mixed layer. Phys Fluids 18. doi:10.1063/1.2337098

Restrepo JM (2007) Wave breaking dissipation in the wave-driven ocean circulation. J Phys Oceanogr 37:1749–1763

Rößler A (2010) Runge-Kutta method for the strong approximation of solutions of stochastic differential equations. Soc Indust Appl Math 48:922–952

Ross ON (2010) Particles in motion: how turbulence affects plankton sedimentation from an oceanic mixed layer. Geophys Res Lett 33. doi:10.1029/2006GL026352

Santamaria F, Boffetta G, Afonso MM, Mazzino A, Onorato M, Pugliese D (2013) Stokes drift for inertial particles transported by water waves. EPL 102. doi:10.1209/0295–5075/102/14003

Svendsen IA (2006) Introduction to nearshore hydrodynamics. Advanced series on ocean engineering 24

Tang W, Taylor J, Mahalov A (2010) Lagrangian dynamics in stochastic inertial-gravity waves. Phys Fluids 22

Tennekes H, Lumely JL (1972) A first course in turbulence. The MIT Press, Cambridge, London, England

Umeyama M (2012) Eulerian-Lagrangian analysis for particle velocities and trajectories in a pure wave motion using particle image velocimetry. Philos Trans R Soc Lond Ser App Math Phys Eng Sci 370:1687–1702

Whitham GB (1974) Linear and nonlinear waves. Wiley, New York

Wiegel RL (1960) A presentation of cnoidal wave theory for practical application. J Fluid Mech 7:273–286

Wilson JD (2000) Trajectory models for heavy particles in atmospheric turbulence: comparison with observations. J Appl Meteor 39:1894–1912